JPE 19-6-5

https://doi.org/10.6113/JPE.2019.19.6.1393
ISSN(Print): 1598-2092 / ISSN(Online): 2093-4718

Power Flow Control of Four Channel Resonant Step-Down Converters

Lilla Litvani* and Janos Hamar†

†,*Dept. of Automation and Applied Informatics, Budapest University of Technology and Economics, Budapest, Hungary

Abstract

This paper proposes a new power flow control method for soft-switched, four channel, five level resonant buck dc-dc converters. These converters have two input channels, which can be supplied from sources with identical or different voltages, and four output channels with arbitrary output voltages. They are specially designed to supply multilevel inverters. The design methodology for their power flow control has been developed considering a general case when the input voltages, output voltages and loads can be asymmetrical. A special emphasize is paid to the limitations and restrictions of operation. The theoretical studies are confirmed by numerical simulations and laboratory tests carried out at various operation points. Exploiting the advantages of the newly proposed power control strategy, the converter can supply five level inverters in dc microgrids, active filters, power factor correctors and electric drives. They can also play an interfacing role in renewable energy systems.

Key words: Design, Multichannel converter, Power flow control, Resonant converter, Soft switching, Step-down dc-dc converter

I. INTRODUCTION

Resonant DC/DC converters have recently drawn a lot of attention in various application fields due to their specific advantages. Among these advantages, zero voltage and zero current switching (ZVS and ZCS), high efficiency, low electromagnetic interference (EMI), improved performance and high power density make them popular in DC microgrids, renewable energy systems and switched mode power supplies. Several papers have been published on different converter topologies for electric vehicles [1]-[3]. In fuel cells, beside a simple control, the power semiconductors require a low voltage stress, while the DC bus needs a higher constant voltage. In order to achieve this, a three-level, H-type structural boost converter was created to provide a wide voltage-gain range [4]. For DC microgrid applications, voltage-balancing and battery state of charge adjusting are important requirements for an applied converter. Several control strategies have been proposed to ensure these criteria [5], [6]. For battery charging applications, a high efficiency design method has been proposed, where lithium-ion battery cells have been used due to their high current and voltage rates, which results in a high power density [7]. A parameter selection method was proposed to implement multi-element resonant converters after four design steps. The achieved converter allowed for an efficiency as high as 96.9% [8].

Since the application field of DC/DC converters is so wide, several different topologies have been presented with various additional advantages. Zero-voltage and zero-current switching topologies allow for a decrease of the switching losses [9]-[11]. In addition to ZVS, voltage regulation can be reached over a wide range of loads by the hybrid control of the frequency and duty ratio, which results in an enlarged conversion efficiency [12]. Using only one active switch, a leakage-energy recycling dual DC/DC flyback converter has been introduced [13]. Another single switch topology has been proposed, where the input source and the clamped capacitor are in series in order to transfer energy towards the load through dual voltage multiplier cells. As a result, the converter is able to produce a very high voltage while having a high conversion efficiency [14]. A reduced-size, two-switch converter was proposed with a non-isolated high voltage gain, which results in a very simple circuit with continuous input current and a small ripple [15]. A parallel loaded resonant converter providing a wide output voltage range was introduced

Manuscript received Feb. 6, 2019; accepted Jun. 27, 2019
Recommended for publication by Associate Editor Jae-Beum Lee.
†Corresponding Author: litvani.lilla@aut.bme.hu
Tel: +36 (1) 463-2337, Budapest University of Technology and Economics
*Dept. Autom. Applied Inform., Budapest Univ. Tech. Economics, Hungary

in [16]. By modifying the transformer turns ratio, it can become applicable in high power environments. A two channel converter family was proposed, where the energy was able to flow from the input to the output within the channels, and also among the two channels. These converters were analyzed in both symmetrical and asymmetrical conditions [17], [18].

This paper proposes a new approach to control the power flow of the four channel buck converter introduced in [19]. Based on experience, the conventional duty ratio based control of this converter faces difficulties since changing the duty ratio of a single switch affects the power flow in multiple channels simultaneously. On the other hand, the newly proposed method enables the direct control of each channel's power flow without any unwanted consequences for the rest of channels. In this paper, general cases of asymmetrical input voltages and output loads are assumed, and the aim is to produce predefined output voltages. This requires overall control of the power exchange among the converter channels. Efficient control strategies are presented for various use-cases. The presented method can be beneficially applied when using a converter to feed five level voltage source inverter (VSI) systems, which facilitates the reduction of their harmonic distortion.

The outline of the paper is as follows. Section II briefly summarizes the operation of a converter, which is crucial to understanding the control strategies. Section III derives a steady state analysis of the converter with energy equations for the discontinuous current conduction mode (DCM). Section IV presents a design method for power flow control. Section V concentrates on the proposed control in partially asymmetrical cases. Control characteristics are presented in Section VI. Section VII shows the simulation and experimental results. Finally, some conclusions are presented in Section VIII.

II. Basic Operation of the Converter

A circuit diagram of a four-channel buck converter can be seen in Fig. 1. The operation of the converter is briefly summarized in this paper. Further information can be found in [19]. During the investigation of the lossless components, ripple free input and output voltages are presumed, and the commutation intervals are neglected among the switches. In the analytical study, one switching cycle is examined, which is built up from three time intervals (*0p*, *1p*, *2p*). T_s is the switching period, and $\omega = \frac{1}{\sqrt{LC}}$ is the resonant angular frequency. Steady-state operating waveforms of the converter in the DCM are shown in Fig. 2. They include the resonant currents i_{Lp} and i_{Ln} of both inductors and the resonant voltage of the switched capacitor v_c.

Interval 0p [$0 < \omega t < \alpha_p$] (see the red continuous line in Fig. 3). Here, the controlled switch S_p is turned on in order to charge the switched capacitor C and to energize the inductor

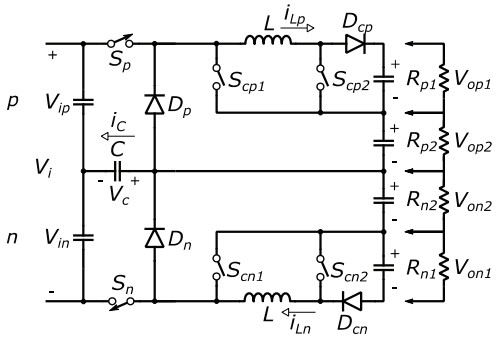

Fig. 1. Four-channel buck converter.

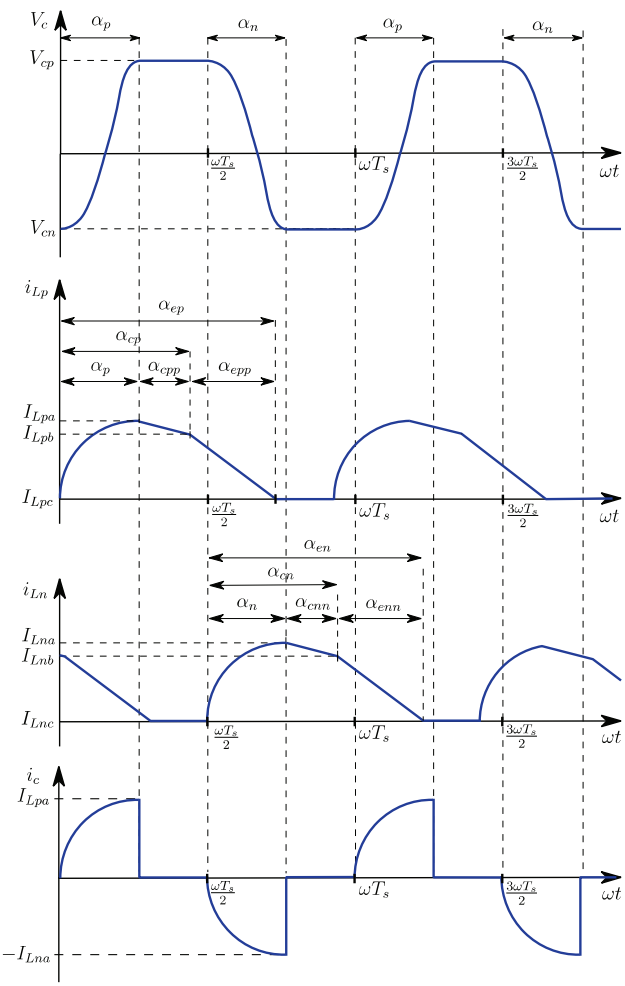

Fig. 2. Time function of the capacitor voltage and inductor current.

L in the positive (p) channel. The switches S_{cp1} and S_{cp2} are turned off. The voltage of the capacitor v_c sinusoidally increases, while the sinusoidal current flows through the circuit V_{ip}-S_p-L-D_{cp}-V_{op1}-V_{op2}-C. The instantaneous value of the inductor current at the end of this interval is $i_c(\alpha_p)=i_{Lp}(\alpha_p)=I_{Lpa}$.

Interval 1p [$\alpha_p < \omega t < \alpha_{cp}$] (see the blue continuous line in Fig. 3). At the beginning of this interval, the controlled switch S_p is turned off, while S_{cp1} is turned on using the energy of L to feed the output. V_c remains constant in this

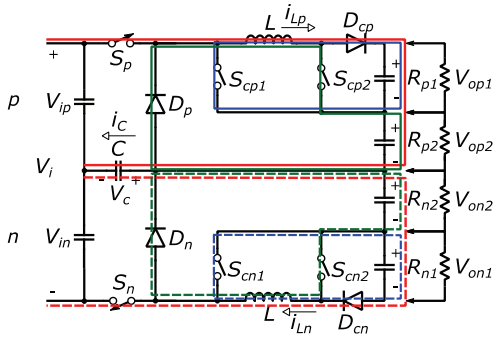

Fig. 3. Current paths during switching intervals.

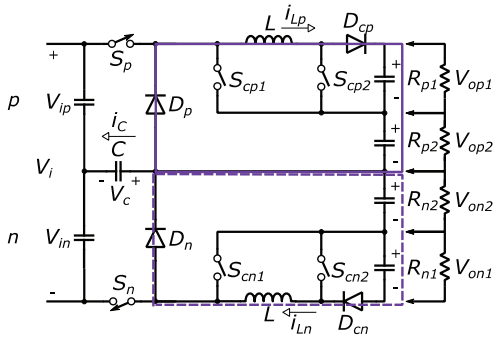

Fig. 4. Protection mode.

interval, while the current flows in the circuit L-D_{cp}-V_{op1}-S_{cp1}. As a result, i_{Lp} linearly decreases, and at the end of this interval $i_{Lp}(\alpha_{cp})=I_{Lpb}$.

Interval 2p [$\alpha_{cp} < \omega t < \alpha_{ep}$] (see the green continuous line in Fig. 3). Both S_p and S_{cp1} are turned off, and S_{cp2} is turned on. When the current is flowing in the circuit L- S_{cp2}-V_{op2}-D_p, all of the energy of the inductor is depleted, and the current i_{Lp} becomes zero at the extinction angle α_{ep}, that is, $i_{Lp}(\alpha_{ep})=I_{Lpc}=0$. It remains in this state until the end of the period T_s. It is important to note, that this only holds true for the discontinuous conduction mode (DCM). In the continuous conduction mode (CCM), the inductor current cannot reach zero before the beginning of the next period.

Additionally, there is a special operational state of the converter, called the protection mode (see the purple continuous line in Fig. 4 for channel p, and the dashed line for channel n), which is due the voltage of the capacitor reaching the input voltage, $V_{cp}=V_{ip}$ (or $V_{cn}=-V_{in}$). In this case, the diode D_p (or D_n) turns on making the inductor's current flow in the circuit L- D_{cp}- V_{op1}-V_{op2} -D_p. The purpose of this operation mode is to avoid overvoltage of the capacitor and to protect the switches in the circuit in case of a failure.

The operation intervals at the negative channel are the same as those written above (see the dashed lines in Fig. 3), only shifted by half a period, $\frac{\omega T_s}{2}$. The output voltages can be directly controlled by the switching frequency $f_s=\frac{1}{T_s}$ or the conduction angles of the controlled switches.

In the paper, positive $x_1=\frac{x_p+x_n}{2}$ and negative $x_2=\frac{x_p-x_n}{2}$ sequence symmetrical components are introduced, where x_p and x_n are the same kind of variables or parameters (e.g. voltages) in channels p and n, respectively. Examples of symmetrical components are as follows: positive sequence input voltage $V_{i1}=\frac{V_{ip}+V_{in}}{2}$ and negative sequence input voltage $V_{i2}=\frac{V_{ip}-V_{in}}{2}$. Since $V_{cn}<0$, the positive sequence capacitor voltage is $V_{c1}=\frac{V_{cp}-V_{cn}}{2}$, and the negative sequence capacitor voltage is $V_{c2}=\frac{V_{cp}+V_{cn}}{2}$. V_{cp} and V_{cn} are the peak values of the capacitor voltage time function (see Fig. 2).

III. Analytical Study Based on Energy Equations

In this section, energy pulse equations are analyzed for one switching period, T_s. The equations are mostly derived for channel p, unless those for channel n are crucial for understanding. However, using the equations of channel p, the corresponding channel n equations can easily be produced by the following formal parameter substitutions: $x_p \leftrightarrow x_n$ (except $V_{cp} \leftrightarrow -V_{cn}$), $x_1 \leftrightarrow x_1$ and $x_2 \leftrightarrow -x_2$. During the analysis, the following per unit parameters are used: $f_s^*=\frac{f_s}{f_r}$, $R^*=\frac{R}{Z}$, $R_{p1}^*=\frac{R_{p1}}{Z}$, $R_{p2}^*=\frac{R_{p2}}{Z}$, $V_{c1}^*=\frac{V_{c1}}{V_{i1}}$, $V_{c2}^*=\frac{V_{c2}}{V_{i1}}$, $V_{ip}^*=\frac{V_{ip}}{V_{i1}}$, $V_{in}^*=\frac{V_{in}}{V_{i1}}$, $V_{op1}^*=\frac{V_{op1}}{V_{i1}}$, $V_{op2}^*=\frac{V_{op2}}{V_{i1}}$, $I_{Lpb}^*=\frac{I_{Lpb}}{I_{base}}$ and $I_{Lpa}^*=\frac{I_{Lpa}}{I_{base}}$, where $f_r=\frac{1}{2\pi\sqrt{LC}}$ is the resonant frequency, $Z=\sqrt{L/C}$ is the characteristic impedance and $I_{base}=\frac{V_{i1}}{Z}$ is the unit of the current. When $R_{p1}=R_{p2}$, $R_{p1}^*=R_{p2}^*=R^*$ and when $V_{op1}=V_{op2}$, $V_{op1}^*=V_{op2}^*=V_{op1,2}^*$.

The total input energy w_{ip} is delivered by the current pulse $i_{cp}=i_{Lp}$ feeding the converter, while $0 < \omega t < \alpha_p$. The input energy taken from source p can be calculated from the capacitor current and voltage as follows:

$$w_{ip}=V_{ip}\int_0^{\alpha_p/\omega} i_c dt = V_{ip}C\left(V_{cp}-V_{cn}\right)=2CV_{ip}V_{c1} \quad (1)$$

Similarly:

$$w_{in}=V_{in}C\left(-V_{cn}+V_{cp}\right)=2CV_{in}V_{c1} \quad (2)$$

Supposing lossless operation, the total input energy is equal to the total output energy:

$$w_i=w_{ip}+w_{in}=w_o=4CV_{c1}V_{i1} \quad (3)$$

Assuming the input voltages remain constant, V_{c1} is a good candidate for controlling the input energy.

The switched capacitor plays an energy steering role among the input channels p and n.

$$\Delta w_{cp}=\frac{C(V_{cp}^2-V_{cn}^2)}{2}=2CV_{c1}V_{c2} \quad (4)$$

The energy that continues toward the output in channel p *(n)* and is dissipated on the loads is:

$$w_{op} = w_{ip} - \Delta w_{cp} = 2CV_{c1}\left(V_{ip} - V_{c2}\right) = \frac{V_{op1}^2}{R_{p1}f_s} + \frac{V_{op2}^2}{R_{p2}f_s} \quad (5)$$

$$w_{on} = w_{in} + \Delta w_{cp} = 2CV_{c1}(V_{in} + V_{c2}) = \frac{V_{on1}^2}{R_{n1}f_s} + \frac{V_{on2}^2}{R_{n2}f_s} \quad (6)$$

The ratio of the energy transferred in channel p, when compared to the total output energy, can be expressed by dividing (5) by (3) as follows:

$$\frac{W_{op}}{W_o} = \frac{2CV_{c1}(V_{ip} - V_{c2})}{4CV_{c1}V_{i1}} = \frac{1}{2}\left(\frac{V_{ip} - V_{c2}}{V_{i1}}\right) = \frac{\frac{V_{op1}^2}{R_{p1}f_s} + \frac{V_{op2}^2}{R_{p2}f_s}}{\frac{V_{op1}^2}{R_{p1}f_s} + \frac{V_{op2}^2}{R_{p2}f_s} + \frac{V_{on1}^2}{R_{n1}f_s} + \frac{V_{on2}^2}{R_{n2}f_s}} \quad (7)$$

similarly:

$$\frac{W_{on}}{W_o} = \frac{2CV_{c1}(V_{in} + V_{c2})}{4CV_{c1}V_{i1}} = \frac{1}{2}\left(\frac{V_{in} + V_{c2}}{V_{i1}}\right) = \frac{\frac{V_{on1}^2}{R_{n1}f_s} + \frac{V_{on2}^2}{R_{n2}f_s}}{\frac{V_{op1}^2}{R_{p1}f_s} + \frac{V_{op2}^2}{R_{p2}f_s} + \frac{V_{on1}^2}{R_{n1}f_s} + \frac{V_{on2}^2}{R_{n2}f_s}} \quad (8)$$

This shows that V_{c2} is a good candidate for controlling the energy exchange among the input channels p and n.

In the DCM, the output energy pulses in channels p_1 and p_2 for the above described intervals, which can be calculated as follows:

$0 < \omega t < \alpha_p$

$$w_{op1}^{(0p)} = \int_0^{\alpha_p/\omega} i_c \cdot V_{op1}\, dt = 2CV_{c1}V_{op1} \quad (9)$$

$$w_{op2}^{(0p)} = \int_0^{\alpha_p/\omega} i_c \cdot V_{op2}\, dt = 2CV_{c1}V_{op2} \quad (10)$$

$\alpha_p < \omega t < \alpha_{cp}$

$$w_{op1}^{(1p)} = \frac{1}{2}L\left(I_{Lpa}^2 - I_{Lpb}^2\right) = w_{Lpa} - w_{Lpb} \quad (11)$$

$$w_{op2}^{(1p)} = 0 \quad (12)$$

$\alpha_{cp} < \omega t < \alpha_{ep}$

$$w_{op1}^{(2p)} = 0 \quad (13)$$

$$w_{op2}^{(2p)} = \frac{1}{2}L\, I_{Lpb}^2 = w_{Lpb} \quad (14)$$

By adding equations (9), (11) and (13) and (10), (12) and (14), the energy transferred through channels p_1 and p_2 and dissipated on the loads can be calculated for one switching period.

$$w_{op1} = 2\, C\, V_{c1}V_{op1} + \frac{1}{2}L\left(I_{Lpa}^2 - I_{Lpb}^2\right) = \frac{V_{op1}^2}{R_{p1}f_s} \quad (15)$$

$$w_{op2} = 2\, C\, V_{c1}V_{op2} + \frac{1}{2}L\, I_{Lpb}^2 = \frac{V_{op2}^2}{R_{p2}f_s} \quad (16)$$

The total output energy of channel p can be calculated by adding equations (15) and (16). This is equal to the energy (w_{op}) supplied to channel p after deducting the capacitor's energy change [see (5)]:

$$w_{op} = 2V_{c1}(V_{op1} + V_{op2}) + \frac{1}{2}LI_{Lpa}^2 = 2CV_{c1}\left(V_{ip} - V_{c2}\right) \quad (17)$$

From (17), I_{Lpa}^2 can be expressed as:

$$I_{Lpa}^2 = 4\frac{C}{L}V_{c1}(V_{ip} - V_{op1} - V_{op2} - V_{c2}) \quad (18)$$

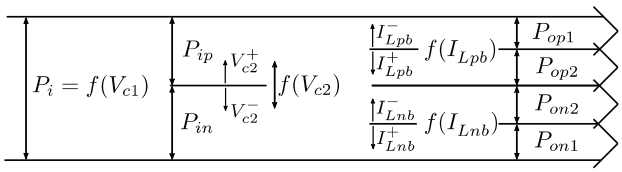

Fig. 5. Power flow from the inputs towards the outputs.

Substituting (18) into (15), the following equation can be expressed for the output energy w_{op1}:

$$w_{op1} = 2\, C\, V_{c1}(V_{ip} - V_{op2} - V_{c2}) - \frac{1}{2}LI_{Lpb}^2 = \frac{V_{op1}^2}{R_{p1}f_s} \quad (19)$$

Equations (16) and (19) indicate that I_{Lpb} is a good candidate to control the energy exchange among output channels p_1 and p_2. Similarly, I_{Lnb} is a good candidate among channels n_1 and n_2.

V_{op2} can be expressed from (16) as follows:

$$V_{op2} = R_{p2}f_sCV_{c1}\left(1 + \sqrt{1 + \frac{L\, I_{Lpb}^2}{2R_{p2}f_sC^2V_{c1}^2}}\right) \quad (20)$$

Substituting (20) into (19), V_{op1} can be calculated as follows:

$$V_{op1} = \sqrt{2CV_{c1}R_{p1}f_s\left(A_1 - \frac{1}{2}LI_{Lpb}^2R_{p1}f_s\right)} \quad (21)$$

where:

$$A_1 = V_{ip} - V_{c2} - R_{p2}f_sCV_{c1}\left(1 + \sqrt{1 + \frac{L\, I_{Lpb}^2}{2\, R_{p2}f_sC^2V_{c1}^2}}\right) \quad (22)$$

Instead of energy pulses, average powers are used exclusively from now on, which can be directly calculated by multiplying the energy pulse values with the switching frequency so that: $P_x = w_x f_s$.

Based on (20) and (21), it can be concluded that the output voltages (and the powers) are determined by the inductor currents I_{Lpb} and I_{Lnb} as well as the positive and negative sequence switched capacitor peak voltages, V_{c1} and V_{c2}. Consequently, these four parameters are considered as the control variables (f_s is kept constant).

Fig. 5 shows how they influence the power flow of the converter. Based on (3), V_{c1} specifies the amount of power fed into the converter. V_{c2} determines how this power is shared among input channels p and n (7) and (8). The inductor currents I_{Lpb} and I_{Lnb} enable the power exchange among output channels p_1, p_2 and n_1, n_2, respectively (16) and (19).

IV. Design Considerations

This section discusses the procedure to design the power flow control. First, the calculation of the control variables V_{c1}, V_{c2}, I_{Lpb} and I_{Lnb} is introduced considering arbitrary steady-state

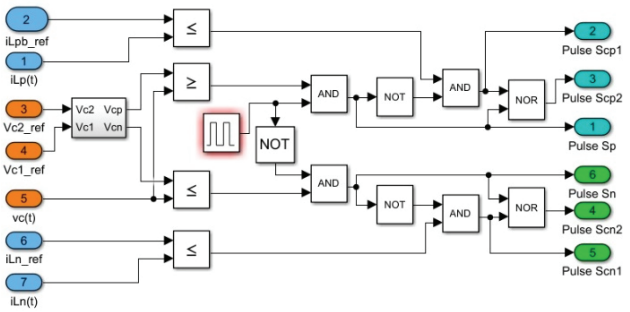

Fig. 6. Generating switching signals.

operation points in the DCM. Afterwards, the steps are explained to decide if the operation point is feasible or not. Fig. 6 shows a circuit block diagram to generate the turn on and turn off signals of the controlled switches. The calculated values of the control parameters are denoted as reference values in the figure [$V_{c1,ref}$, $V_{c2,ref}$, $I_{Lpb,ref}$ and $I_{Lnb,ref}$], which are compared to the instantaneous values of the respective variables during the operation [$v_c(t)$, $i_{Lp}(t)$ and $i_{Ln}(t)$]. Thus, the turn-on and turn-off intervals of the switches are indirectly controlled.

A. Calculation of Power Flow Control Parameters

The values of L and C determine the resonant frequency. Since the two input currents can only flow in separate intervals, the simultaneous turn-on of the controlled switches S_p and S_n must be avoided. This can be accomplished by choosing the switching frequency so that: $f_s \le f_r$. On the other hand, an increase of f_s is preferred to reduce the output voltage ripple and to avoid degradation of the dynamical performance of the converter. Hence, the switching frequency is chosen as: $f_s = f_r = \frac{1}{2\pi\sqrt{LC}}$.

For the design, prior knowledge of the following parameters is assumed from the system specifications: V_{ip}, V_{in}, V_{op1}, V_{op2}, V_{on1}, V_{on2}, R_{p1}, R_{p2}, R_{n1} and R_{n2}.

The four output powers can be easily calculated by using the well-known equation: $P_{ox} = \frac{V_{ox}^2}{R_x}$.

Since lossless circuit components are assumed, the total input energy (average power) is equal to the total output energy (power), w_i=w_o and P_i=P_o. This power is determined by the control variable V_{c1}, which can be expressed from (3) as follows:

$$V_{c1} = \frac{P_o}{4Cf_sV_{i1}} = \frac{P_{op1}+P_{op2}+P_{on1}+P_{on2}}{4Cf_sV_{i1}} \quad (23)$$

The power exchange among the input channels p and n is controlled by the variable V_{c2}, which can be expressed from (7):

$$V_{c2} = V_{ip} - \frac{2V_{i1}(P_{op1}+P_{op2})}{P_{op1}+P_{op2}+P_{on1}+P_{on2}} \quad (24)$$

The control parameter I_{Lpb} can be calculated from (16) using (3).

$$I_{Lpb} = \sqrt{\frac{2P_{op2}-\frac{P_oV_{op2}}{V_{i1}}}{Lf_s}} \quad (25)$$

Similarly, I_{Lnb} is:

$$I_{Lnb} = \sqrt{\frac{2P_{on2}-\frac{P_oV_{on2}}{V_{i1}}}{Lf_s}} \quad (26)$$

B. Operation Limits

Various operational limits need to be taken into consideration when designing the control. The peak voltages of the capacitor are limited by the available maximum commutation angles $\alpha_p = 180°$ and $\alpha_n = 180°$. In this case, the capacitor current and the choke current waveforms are half sinusoidal. In addition, the instantaneous values of the currents I_{Lpa} and I_{Lpb} (and similarly I_{Lna} and I_{Lnb}) are zero (see Fig. 2). By substituting I_{Lpa} = I_{Lpb} =*0* into (15) and (16) (and similarly I_{Lna} = I_{Lnb} =*0* into the n channel equivalent equations), the capacitor voltage V_{c1} is limited as follows:

$$0 < V_{c1} < V_{c1}^{max} = min\left\{\frac{V_{op1}\pi}{R_{p1}^*f_s^*}, \frac{V_{op2}\pi}{R_{p2}^*f_s^*}, \frac{V_{on1}\pi}{R_{n1}^*f_s^*}, \frac{V_{on2}\pi}{R_{n2}^*f_s^*}\right\} \quad (27)$$

By substituting I_{Lpa}=*0* into (18) (and similarly I_{Lna} = *0* into the n channel equivalent equation), the limitations of V_{c2} can be obtained as follows:

$$-(V_{in} - V_{on1} - V_{on2}) \le V_{c2} \le V_{ip} - V_{op1} - V_{op2} \quad (28)$$

The inductor currents I_{Lpb} and I_{Lnb} have a limit since they cannot be higher than I_{Lpa} and I_{Lna} (see Fig. 2), respectively. From (18):

$$0 \le I_{Lpb} \le \frac{2}{Z}\sqrt{V_{c1}(V_{ip} - V_{op1} - V_{op2} - V_{c2})} \quad (29)$$

$$0 \le I_{Lnb} \le \frac{2}{Z}\sqrt{V_{c1}(V_{in} - V_{on1} - V_{on2} + V_{c2})} \quad (30)$$

The converter operates in the *protection mode* when V_{cp}=V_{ip} or V_{cn}=-V_{in}. To allow for the proper control of the converter, the protection mode has to be avoided. Thus, $V_{cp} \le V_{ip}$ and $V_{cn} \ge -V_{in}$.

V. Special Asymmetrical Cases

To reveal the effects of control variables, the following special asymmetrical cases are examined: asymmetrical output voltages, asymmetrical loads and asymmetrical input voltages. At the same time, only one quantity is considered to be asymmetrical, while the remaining ones are considered to be symmetrical. The relating control characteristics are discussed in Section VI.

A. Asymmetrical Output Voltages

At this point, V_{op1}≠V_{op2}. However, V_{op1}=V_{on1}, V_{op2}=V_{on2}, V_{ip}=V_{in} and R_{p1}=R_{p2}=R_{n1}=R_{n2}. Substituting them into (7) and since V_{ip}=V_{i1}, it follows that V_{c2}=*0*. Substituting the per unit

values into (16), I_{Lpb}^* in the function of V_{op2}^* can be calculated as:

$$I_{Lpb}^* = \sqrt{4\left(\frac{V_{op2}^{*2}\pi}{R^* f_s^*} - V_{c1}^* V_{op2}^*\right)} \quad (31)$$

Substituting the per unit values into (21), I_{Lpb}^* can also be calculated in the function of V_{op1}^* as:

$$I_{Lpb}^* = \sqrt{\frac{-A_2 - \sqrt{{A_2}^2 - 4A_3}}{2}} \quad (32)$$

where:

$$A_2 = -8V_{c1}^* + \frac{8\pi V_{op1}^{*2}}{R^* f_s^*} \quad (33)$$

$$A_3 = 16V_{c1}^{*2} - \frac{32\pi V_{op1}^{*2} V_{c1}^{*2}}{R^* f_s^*} - 16R^* f_s^* V_{c1}^{*3} + \frac{16\pi V_{op1}^{*2}}{R^{*2} f_s^{*2}} + A_4 \quad (34)$$

where:

$$A_4 = 16V_{c1}^{*2} V_{op1}^{*2} \quad (35)$$

B. Asymmetrical Loads

At this point, the case where $R_{p1} \neq R_{p2}$, but $R_{p1}=R_{n1}$, $R_{p2}=R_{n2}$, $V_{ip}=V_{in}=V_{i1}$ and $V_{op1}=V_{op2}=V_{on1}=V_{on2}$ is investigated. Based on (7) $V_{c2}=0$.

Substituting the per unit values into (16), I_{Lpb}^* in function of R_{p2}^* can be calculated as:

$$I_{Lpb}^* = \sqrt{4\left(\frac{V_{op1,2}^{*2}\pi}{R_{p2}^* f_s^*} - V_{c1}^* V_{op1,2}^*\right)} \quad (36)$$

Similarly, I_{Lpb}^* as a function of R_{p1}^* can be expressed from (21) as:

$$I_{Lpb}^* = \sqrt{4\left(V_{c1}^*(1 - V_{op1,2}^*) - \frac{V_{op1,2}^{*2}\pi}{R_{p1}^* f_s^*}\right)} \quad (37)$$

C. Asymmetrical Input Voltages

In this case, $V_{ip} \neq V_{in}$, $V_{op1}=V_{op2}=V_{on1}=V_{on2}$, $R_{p1}=R_{p2}=R_{n1}=R_{n2}$ and all of the output powers are identical. At this point, $\frac{P_{op}}{P_o} = \frac{1}{2}$ is based on (7) and:

$$V_{c2}=V_{i2} \quad (38)$$

This shows that the asymmetry in the input voltages can be efficiently compensated by V_{c2}.

The output power (and voltage) can be controlled by V_{c1} [see (23)]:

$$P_o = \frac{4V_{op1}^2}{R_{p1}} = 4Cf_s V_{c1} V_{i1} \quad (39)$$

I_{Lpb} and I_{Lnb} are determined by (25) and (26). As long as V_{i1} remains constant, no adjustment is required at these control variables. If V_{i1} changes, I_{Lpb} and I_{Lnb} need to be adjusted accordingly.

D. Symmetrical Operation Points

As a special case, symmetrical operation points can also be realized, by considering that all of the circuit and control parameters are identical in the p and n sides. V_{c1} can be expressed using (23):

$$V_{c1,symm}^* = \frac{2\pi V_{op1,2}^{*2}}{R^* f_s^*} \quad (40)$$

In symmetrical operation, all of the negative sequence components are zero. As a result, V_{c2} is also zero. By subtracting (19) from (16), the control parameter I_{Lpb}^* can be calculated as follows:

$$I_{Lpb,symm}^* = \sqrt{2V_{c1}^*\left(1 - 2V_{op1,2}^*\right)} \quad (41)$$

The ratio of the currents I_{Lpb}^* and I_{Lpa}^* can also be calculated. Squaring (41), dividing it by (18) and substituting the per unit values yields:

$$\frac{I_{Lpb}^{*2}}{I_{Lpa}^{*2}} = \frac{2V_{c1}^*(1-2V_{op1,2}^*)}{4V_{c1}^*(1-2V_{op1,2}^*)} = \frac{1}{2} \quad (42)$$

As expected, this ratio gives 0.5 since half of the energy is delivered to the output p_1 and half to p_2. The situation is also the same in channel n.

VI. Asymmetrical Control Characteristics

This section is concerned with the relationships among the output voltages, input voltages and control variables. As the steady state analysis pointed out, during asymmetrical conditions, the capacitor peak voltages V_{c1}^* and V_{c2}^* and the inductor currents I_{Lpb}^* and I_{Lnb}^* are appropriate parameters to control the output voltages and powers. Various scenarios are examined, including changes of the loads and the input voltages of the system. The characteristic curves were calculated in MATLAB R2018b. Numerous operation points were selected and marked with capital letters A-I, and simulations and laboratory measurements were carried (see Table I). In the characteristics, the green curves indicate symmetrical operation, while the black curves represent the protection mode and further operational limits. The continuous lines mark the channel p (or $p1$) parameters, while the dashed lines represent the channel n (or $p2$) parameters.

A. Change of the Output Voltage

Fig. 7 shows the effects of output voltage changes during constant and symmetrical loads and input voltages in the control plain set-up by V_{c1} and I_{Lpb}. The point G represents a symmetrical operation point. Moving from G to C, V_{op1}^* remains constant, while V_{op2}^* increases by a factor of 1.6 when compared to its value at point G. By increasing both of the control variables, a new stable operation point is reached. Fig. 8 represents one of the advantages of the proposed control method. $V_{c1}^*=1$ is reached during operation that gives immediate information that protection mode is reached and V_{c1}^* cannot be increased any further as shown in point D. This

TABLE I
SELECTED OPERATION POINTS FOR ASYMMETRICAL OPERATION, DCM, WHERE f_S^*=1

		R_{p1}^*[pu]	R_{p2}^*[pu]	V_{ip}^*[pu]	V_{in}^*[pu]	V_{c1}^*[pu]	V_{c2}^*[pu]	I_{Lpb}^*[pu]	I_{Lnb}^*[pu]
A	asym load	6.0	3	1.00	1.00	0.10	0.00	0.40	0.40
B	asym load	1.5	3	1.00	1.00	0.20	0.00	0.26	0.26
C	asym outp. voltage	1.5	1.5	1.00	1.00	0.47	0.00	0.78	0.78
D, prot	asym outp. voltage	0.8	0.8	1.00	1.00	1.00	0.00	0.52	0.52
E	asym input	1.5	1.5	0.40	1.60	0.26	-0.60	0.51	0.51
F	asym input	1.5	1.5	1.30	0.67	0.26	0.33	0.51	0.51
G	sym	1.5	1.5	1.00	1.00	0.26	0.00	0.52	0.52
H	fully asym	0.6	0.8	0.86	1.14	0.30	-0.10	0.63	0.63

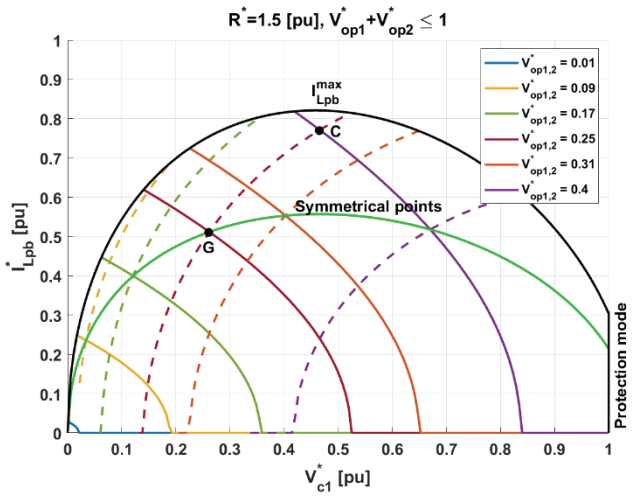

Fig. 7. Control characteristics $V_{op1,2}^*(V_{c1}^*,I_{Lpb}^*)$,$R^*$=1.5.

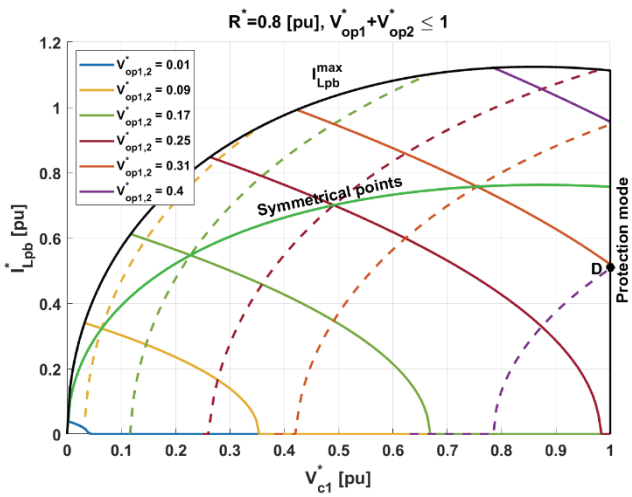

Fig. 8. Control characteristics $V_{op1,2}^*(V_{c1}^*,I_{Lpb}^*)$,$R^*$=0.8.

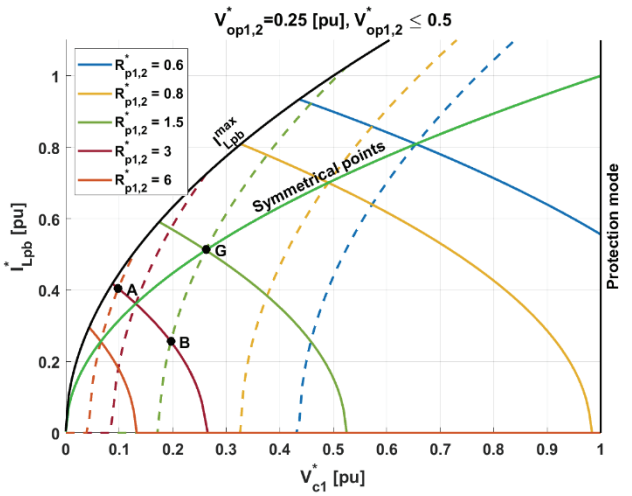

Fig. 9. Control characteristics $R_{p1,2}^*(V_{c1}^*,i_{Lpb}^*)$,$V_o^*$=0.25.

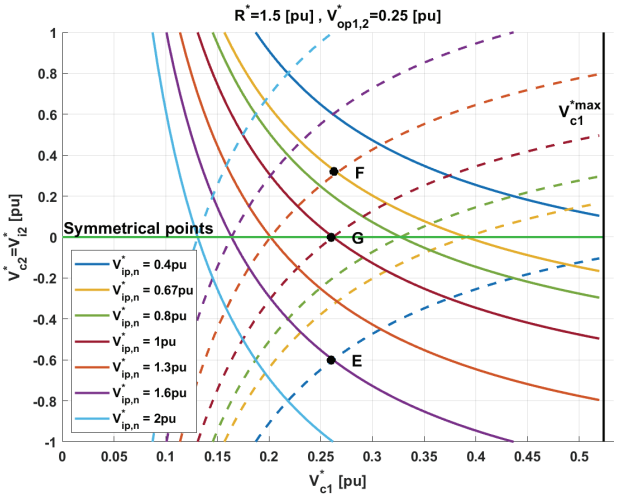

Fig. 10. Control characteristics $V_{ip,n}^*(V_{c1}^*,V_{c2}^*)$,$V_o^*$=0.25,$R^*$=1.5.

also means that the total transferred power cannot be elevated any more.

B. Change of the Load

Fig. 9 represents the effects of load changes at a constant output voltage and input voltage. Assuming starting from the symmetrical operation point G, one of the load resistances, e.g. R_{p2}^* increases from 1.5 to 3. Although the operation becomes asymmetrical, by lowering the values of the control variables to $V_{c1}^* = 0.2$ and $I_{Lpb}^* = 0.26$, the same output voltage $V_{op1,2}^* = 0.25$ can be maintained (B) like the original one. Here, due to the elevated resistance R_{p2}^* (note that $V_{op1,2}^*$ is kept constant), the total output power is decreased, which was achieved by lowering V_{c1}. On the other hand, the ratio of

TABLE II
COMPARISON OF THEORETICAL, SIMULATION AND EXPERIMENTAL RESULTS

	I_{Lpb} [A]			I_{Lnb}[A]			V_{cp}[V]			V_{cn}[V]			V_{op1}[V]			V_{op2}[V]		
	Calc.	Sim.	Lab.	Calc.	Sim.	Lab.	Calc.	Sim.	Lab.	Calc.	Sim.	Lab.	Calc.	Sim.	Lab.	Calc.	Sim.	Lab.
A	2.55	2.55	2.52	2.55	2.55	2.47	1.97	1.98	2.35	-1.98	-1.98	-2.22	5.03	5.08	5.00	4.99	5.00	4.99
B	1.61	1.61	1.45	1.61	1.61	1.52	3.93	3.95	4.12	-3.93	-3.95	-4.30	4.98	4.99	4.90	5.00	5.01	4.90
C	4.91	4.91	5.10	4.91	4.91	4.08	9.38	9.40	8.88	-9.38	-9.40	-9.62	4.98	5.01	4.80	8.00	7.99	7.70
D	3.26	3.19	3.35	3.26	3.19	3.30	20.36	20.10	19.63	-20.36	-20.10	-20.50	8.00	7.93	6.70	6.20	6.15	4.70
E	2.02	2.02	1.95	2.02	2.02	1.98	-4.21	-4.20	-4.25	-10.79	-10.80	-11.25	3.14	3.15	2.90	3.13	3.13	2.80
F	2.43	2.43	2.40	2.43	2.43	2.38	8.95	8.97	9.31	1.05	1.04	1.00	3.76	3.78	3.50	3.76	3.76	3.50
G	3.26	3.25	2.80	3.26	3.26	2.78	5.28	5.30	5.38	-5.28	-5.30	-5.38	4.99	5.01	4.80	5.01	5.00	4.80
H	3.46	3.47	3.45	3.47	3.48	3.25	3.58	3.60	4.13	-7.12	-7.13	-8.13	2.80	2.81	2.67	3.50	3.50	3.70

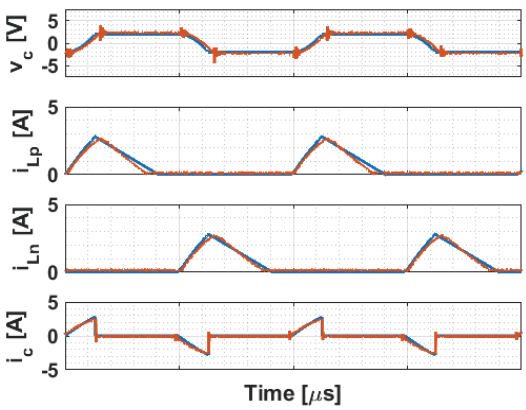

Fig. 11. Time functions at operation point A, where the time unit is 2μsec/Div (blue: simulated; red: measured).

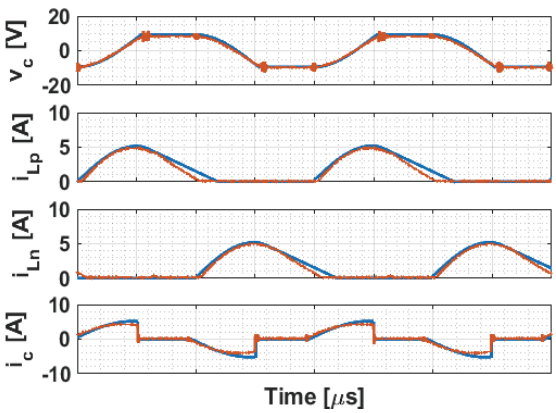

Fig. 12. Time functions at operation point C, where the time unit is 1μsec/Div (blue: simulated; red: measured).

the power balance $\frac{P_{op1}}{P_{op2}}$ is increased, which was achieved by lowering I_{Lpb} (see Fig. 5). At operation point A, the current of the inductor is close to the limitation.

C. Change of the Input Voltage

Fig. 10 shows how changes of the input voltage affect the control characteristics. Here the voltage of the capacitor reaches its maximum (V_{c1}^{*max}) before the protection mode. From the symmetrical operation mode G, if the voltage V_{ip}^* gets higher (or V_{in}^* lower), a stable operation point (F) with symmetrical output voltages ($V_{op1,2}$=$V_{on1,2}$) can be ensured by keeping V_{c1}^*=*const.*

On the other hand, if V_{ip}^* gets smaller (or V_{in}^* gets larger), when V_{c1}^*=*const.*, symmetrical output voltages can be accomplished with $V_{c2}^* = V_{i2}^* \leq 0$ (operation point E). V_{c2} controls the power flow among the input channels *p* and *n*.

VII. SIMULATION AND EXPERIMENTAL VERIFICATION

The considerations and analyses introduced above were tested in both simulation and laboratory environments.

The simulation was run in MATLAB Simulink 2018Rb. A 100W prototype of the converter was built with the following circuit parameters: C=*1 μF*, C_i=*10 μF*, C_o=*200 μF* and L=*10 μH*. Here, the resonant frequency is f_r=*50.329 kHz*. The input voltage range of the converter is *1-24V* for both the *p* and *n* channels, the output voltage range of the converter is also the same. IRF530NPB MOSFETs and STTH802 diodes were used, while the open loop control was realized by a TMS320F283790 DSP. The asymmetrical operation of the converter was tested under numerous control parameter combinations considering changes of the load, input voltage and output voltage. The input voltage was chosen to be V_{ip}=V_{in}=*20V,* except at operation points E (V_{ip}=*5V*, V_{in}=*20V*) and F (V_{ip}=*20V*, V_{in}=*10V*). A comparison of the theoretical, simulation and experimental results can be seen in Table II. Figs. 11-15 show steady-state waveforms of the capacitor voltage $v_c(t)$, inductor currents $i_{Lp}(t)$ and $i_{Ln}(t)$, and capacitor current $i_c(t)$. The red waveforms represent experimental results, while the blue ones show simulation outcomes. Fig. 11 shows the time functions at operation point A when the load is asymmetrical. Fig. 12. presents the effects of asymmetrical output voltages at operation point C. Fig. 13 represents operation point D, which is at the border of the protection mode. Consequently, the capacitor peak voltage just reaches the input voltage level. Fig. 14 demonstrates operation point E, where the input voltages are asymmetrical.

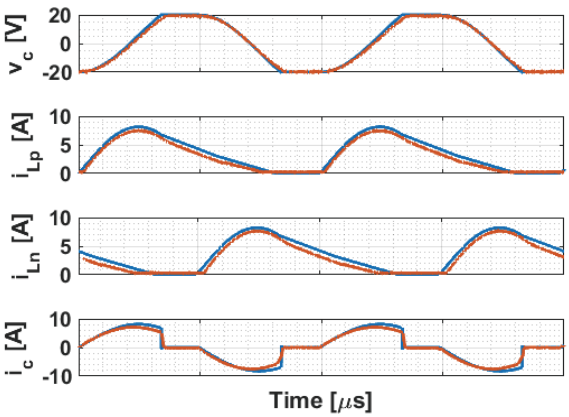

Fig. 13. Time functions at operation point D, where the time unit is 2μsec/Div (blue: simulated; red: measured).

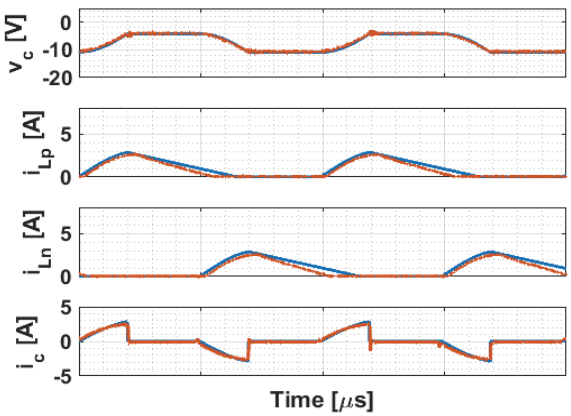

Fig. 14. Time functions at operation point E, where the time unit is 2μsec/Div (blue: simulated; red: measured).

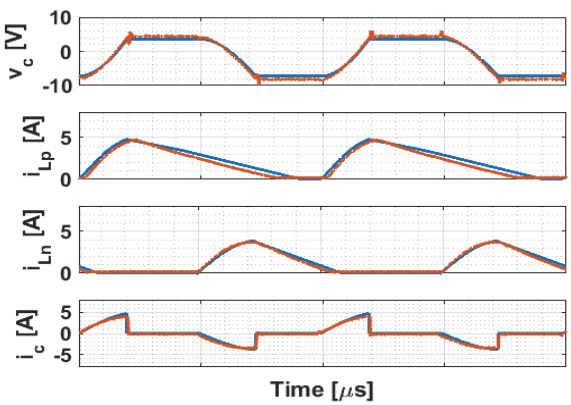

Fig. 15. Time functions at operation point H, where the time unit is 2μsec/Div (blue: simulated; red: measured).

Consequently, $V_{c2} \neq 0$, which means that $V_{cp} \neq -V_{cn}$. Fig. 15 illustrates fully asymmetrical operation at point H.

The compared theoretical and simulation results are practically the same. In addition, laboratory tests are also in good agreement. Small deviations of the latter were due to voltage drops of the real diodes, non-ideal circuit elements and non-linear behavior of the semiconductor switches and passive components.

VIII. Conclusion

A new power flow control has been proposed for a four channel resonant buck converter, while operated in the zero current switching (ZCS) mode. Control of the output voltages and powers were achieved through control variables such as the inductor currents and the peak voltage levels of the capacitor. The switching frequency was fixed at its maximal value, which was determined by the resonant frequency. The new control strategy provides an excellent opportunity to control the total transferred power (by V_{c1}), the exchange of power among the input channels p and n (by V_{c2}) and the power exchange among the output channels p_1 and p_2 [n_1 and n_2] (by I_{Lpb} [I_{Lnb}]). Numerous operation points have been examined in order to verify the theory of the power flow control. Both tests and simulation results have been presented to confirm and verify the theoretical considerations.

Acknowledgment

Project no. FIEK_16-1-2016-0007 has been implemented with the support provided from the National Research, Development and Innovation Fund of Hungary, financed under the Centre for Higher Education and Industrial Cooperation - Research infrastructure development (FIEK_16) funding scheme. The research reported in this paper has also been supported by the National Research, Development and Innovation Fund (TUDFO/51757/2019-ITM, Thematic Excellence Program).

References

[1] W. Sun, X. Jin, L. Zhang, H. Hu, and Y. Xing, "Analysis and design of a multi-resonant converter with a wide output voltage range for EV charger applications," *J. Power Electron.*, Vol. 17, No. 4, pp. 849-859, Jul. 2017.

[2] N. Hassan, Y.-J. Kim, B.-M. Han, and J.-Y. Lee, "A hybrid DC/DC converter for EV OBCs using full-bridge and resonant converters with a single transformer," *J. Power Electron.*, Vol. 17, No. 4, pp. 849-859, Jul. 2017.

[3] H.-N. Vu and W. Choi, "A novel dual full-bridge LLC resonant converter for CC and CV charges of batteries for electric vehicles," *IEEE Trans. Ind. Electron.*, Vol. 65, No. 3, pp. 2212-2225, Mar. 2018.

[4] H. Bi, P. Wang, and Y. Che, "Structural boost three-level DC-DC converter with wide voltage-gain range for fuel cell applications," *J. Power Electron.*, Vol. 18, No. 5, pp. 1303-1314, Sep. 2018.

[5] T. Ahmadi, M. Hamzeh, and E. Rokrok, "Hierarchical control scheme for three-port multidirectional DC-DC converters in bipolar DC microgrids," *J. Power Electron.*, Vol. 18, No. 5, pp. 1595-1607, Sep. 2018.

[6] B. Xie, J. Wang, Y. Jin, Y. Ji, and C. Ma, "Power distribution control scheme for a three-phase interleaved DC/DC converter in the charging and discharging processes of a battery energy storage system," *J. Power Electron.*, Vol. 18, No. 4, pp. 1211-1222, Jul. 2018.

[7] S. Cetin, "High efficiency design procedure of a second stage phase shifted full bridge converter for battery charge applications based on wide output voltage and load ranges," *J. Power Electron.*, Vol. 18, No. 4, pp. 975-984, Jul. 2018.
[8] Y. Wang, L. Yang, G. Li, and S. Tu, "A parameter selection method for multi-element resonant converters with a resonant zero point," *J. Power Electron.*, Vol. 18, No. 2, pp. 332-342, Mar. 2018.
[9] Z.-Y. Chen and Y. Chen, "A secondary resonance soft switching half bridge DC-DC converter with an inductive output filter," *J. Power Electron.*, Vol. 17, No. 6, pp. 1391-1401, Nov. 2017.
[10] M.-K. Nguyen, T.-D. Duong, Y.-C. Lim, and J.-H. Choi, "Active CDS-clamped L-type current-fed isolated DC-DC converter," *J. Power Electron.*, Vol. 18, No. 4, pp. 955-964, Jul. 2018.
[11] M. Yaqoob, K.-H. Loo, and Y. M. Lai, "Fully soft-switched dual-active-bridge series-resonant converter with switched-impedance-based power control," *IEEE Trans. Power Electron.*, Vol. 33, No.11, pp. 9267-9281, Nov. 2018.
[12] H. M. Suryawanshi, S. Pachpor, T. Ajmal, G. G. Talapur, S. Sathyan, M. S. Ballal, V. B. Borghate, and M. R. Ramteke, "Hybrid control of high-efficient resonant converter for renewable energy system," *IEEE Trans. Ind. Informat.*, Vol. 14, No. 5, pp. 1835-1845, May 2018.
[13] L.-S. Yang, "Novel dual DC-DC flyback converter with leakage-energy recycling," *J. Power Electron.*, Vol. 18, No.4, pp. 1007-1014, Jul. 2018.
[14] X. Hu, B. Gao, Y. Huang, and H. Chen, "Novel single switch DC-DC converter for high step-up conversion ratio," *J. Power Electron.*, Vol. 18, No. 3, pp. 662-671, May 2018.
[15] M.-K. Nguyen, Y.-O. Choi, G.-B. Cho, and Y.-C. Lim, "Two-switch non-isolated step-up DC-DC converter," *J. Power Electron.*, Vol. 18, No. 3, pp. 651-661, May 2018.
[16] M. Kim, H. Jeong, B. Han, and S. Choi, "New parallel loaded resonant converter with wide output voltage range," *IEEE Trans. Power Electron.*, Vol. 33, No. 4, pp. 3106-3114, Apr. 2018.
[17] J. Hamar and I. Nagy, "Control features of dual-channel DC-DC converters," *IEEE Trans. Ind. Electron.*, Vol. 49, No. 6, pp. 1293-1305, Dec. 2002.
[18] J. Hamar and I. Nagy, "Asymmetrical operation of dual channel resonant DC-DC converters," *IEEE Trans. Power Electron.*, Vol. 18, No. 1, pp. 83-94, Jan. 2003.
[19] L. Litvani and J. Hamar, "New five level resonant DC/DC buck converter," in *Proceeding of IEEE Power Electronics and Motion Control Conference (IEEE-PEMC)*, pp. 1006-1011, 2018.

Lilla Litvani received her M.S. degree in Electrical Engineering from the Budapest University of Technology and Economics, (BME), Budapest, Hungary, in 2015, where she is presently working towards her Ph.D. degree in the Department of Automation and Applied Informatics. Her current research interests include the modelling, analysis, control and optimization of power converters and DC microgrids.

Janos Hamar received his M.S. and Ph.D. degrees from the Budapest University of Technology and Economics, Budapest, Hungary, in 1998 and 2002, respectively. He was a Research Fellow at the Hungarian Academy of Sciences, Budapest, Hungary, from 1998 to 2001. Later, he worked as a Development Engineer for Exendis Industrie Automation GmbH, Freiburg, Germany. From 2004 to 2006, he was a Research Fellow at Utsunomiya University, Utsunomiya, Japan. He is presently working as an Associate Professor at the Budapest University of Technology and Economics. His current research interests include the modelling, analysis, control and optimization of power converters.